ACCEPTED FOR PUBLICATION IN THE ASTROPHYSICAL JOURNAL
Preprint typeset using LaTeX style emulateapj v. 11/10/09

arXiv:1007.3280v3 [astro-ph.HE] 13 Aug 2010

SUZAKU X-RAY SPECTRA AND PULSE PROFILE VARIATIONS DURING THE SUPERORBITAL CYCLE OF LMC X-4

LI-WEI HUNG[1,2], RYAN C. HICKOX[2,3], BRAM S. BOROSON[2], SAEQA D. VRTILEK[2]

Accepted for publication in The Astrophysical Journal

ABSTRACT

We present results from spectral and temporal analyses of *Suzaku* and *RXTE* observations of the high-mass X-ray binary LMC X-4. Using the full 13 years of available *RXTE*/all-sky monitor data, we apply the ANOVA and Lomb Normalized Periodogram methods to obtain an improved superorbital period measurement of 30.32 ± 0.04 days. The phase-averaged X-ray spectra from *Suzaku* observations during the high state of the superorbital period can be modeled in the 0.6–50 keV band as the combination of a power law with $\Gamma \sim 0.6$ and a high-energy cutoff at $\sim$25 keV, a blackbody with $kT_{\rm BB} \sim 0.18$ keV, and emission lines from Fe K$_\alpha$, O VIII, and Ne IX (X Lyα). Assuming a distance of 50 kpc, the source has luminosity $L_{\rm X} \sim 3 \times 10^{38}$ erg s^{-1} in the 2–50 keV band, and the luminosity of the soft (blackbody) component is $L_{\rm BB} \sim 1.5 \times 10^{37}$ erg s^{-1}. The energy-resolved pulse profiles show single-peaked soft (0.5–1 keV) and hard (6–10 keV) pulses but a more complex pattern of medium (2–10 keV) pulses; cross-correlation of the hard with the soft pulses shows a phase shift that varies between observations. We interpret these results in terms of a picture in which a precessing disk reprocesses the hard X-rays and produces the observed soft spectral component, as has been suggested for the similar sources Her X-1 and SMC X-1.

Subject headings: accretion, accretion disks — pulsars: individual (LMC X-4) — stars: neutron — X-rays: binaries

1. INTRODUCTION

An X-ray binary system consists of a normal star orbiting a compact object (neutron star or black hole) to which the normal star transfers matter either by overflowing its Roche lobe or via a stellar wind. X-ray pulsars are a class of X-ray binaries in which the neutron star has a strong magnetic field, so that accreting matter follows the field lines and falls into the magnetic poles, generating pulses as the magnetic poles rotate in and out of our line of sight. While the general picture of the accretion mechanism is well known, the physics of accretion near the magnetosphere, where the neutron star's magnetic field begins to dominate the flow, is not fully understood. By studying individual X-ray pulsars in detail, we hope to gain a better understanding of the accretion mechanism.

In this paper, we study the X-ray pulsar LMC X-4, which is a high-mass X-ray binary system consisting of a 1.25 $M_\odot$ neutron star accreting from a 14.5 $M_\odot$ O8 III companion (Kelley et al. 1983; van der Meer et al. 2007). The neutron star rotates with a period of $\sim$13.5 s, and orbits its companion with a period of $\sim$1.4 days (White 1978). In addition to the pulse period and the orbital period, the system has been observed to have a long-term period of 30.5 ± 0.5 days (Lang et al. 1981). Between the high and low states of this long-term "superorbital" period (believed to be caused by a precessing accretion disk that periodically obscures the neutron star), the X-ray flux varies by 2 orders of magnitude (Heemskerk & van Paradijs 1989; Naik & Paul 2003). The spectrum of LMC X-4 in the 0.1–100 keV band is well described by a hard power law with a high-energy cutoff, a soft X-ray excess, and a strong iron emission line (Naik & Paul 2003; La Barbera et al. 2001).

Hickox et al. (2004) showed that a soft X-ray excess was a common, and possibly ubiquitous, feature of X-ray pulsars, and that in high-luminosity systems (with $L_X \gtrsim 10^{36}$ erg s^{-1}), the soft excess originates from reprocessing of hard X-rays from the neutron star by the inner accretion disk (Figure 1). This interpretation had been put forward previously to explain the emission from several X-ray pulsars; for example, Burderi et al. (2000) suggested that in Cen X-3, a soft excess below 1 keV originates from reprocessing of the primary radiation by an opaque shell located at the magnetosphere. In this picture, the soft X-rays may be expected to show pulsations that differ in shape and phase from the hard X-ray pulses. Endo et al. (2000) showed that the precessing accretion disk in the X-ray pulsar Her X-1 reprocessed hard X-rays ($>$ 2 keV) from the pulsar and emitted soft X-rays ($<$ 1 keV), and Zane et al. (2004) showed that the phase difference between hard and soft pulses changed as the accretion disk precesses. For the X-ray pulsar SMC X-1, a high-mass X-ray binary similar to LMC X-4, Neilsen et al. (2004) suggested an explanation for the observed characteristics of the soft pulses in terms of precession of the accretion disk. Hickox & Vrtilek (2005) used a model of a twisted inner disk, illuminated by the rotating X-ray pulsar beam, to simulate pulsations in the soft component due to this reprocessing. They found that for some disk and beam geometries, precession of an illuminated accretion disk can roughly reproduce the soft pulse profiles. However, modeling the disk geometry of SMC X-1 is difficult since its superorbital period changes with time. The superorbital period of LMC X-4 is more stable and hence may allow a better test of this picture.

In this paper, we study the X-ray spectra and pulse properties of LMC X-4 at three different phases in the high state of its superorbital cycle. First, we determine an improved value for the superorbital period based on 13 years of *Rossi X-Ray Timing Explorer* (*RXTE*) all-sky monitor (ASM) data and use it to accurately determine the superorbital phase of our three

---

[1] Department of Astronomy, The Ohio State University, McPherson Laboratory 140 W 18th Avenue, Columbus, Ohio 43210-1173, USA; hung.88@buckeyemail.osu.edu

[2] Harvard-Smithsonian Center for Astrophysics, 60 Garden Street, Cambridge, MA 02138, USA; rhickox@cfa.harvard.edu, bboroson@cfa.harvard.edu, svrtilek@cfa.harvard.edu.

[3] Department of Physics, Durham University, South Road, Durham, DH1 3LE, UK

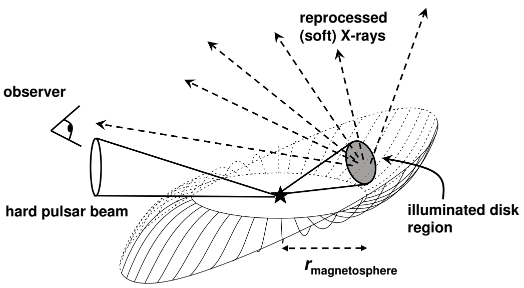

FIG. 1.— Schematic of disk reprocessing in X-ray pulsars (Hickox & Vrtilek 2005). The hard (power-law spectrum) X-ray beam sweeps around and illuminates the accretion disk, which re-radiates a soft X-ray (blackbody) component. The observer sees pulses from both power-law and blackbody components, but these differ in pulse shape and phase.

Suzaku observations. We then analyze the phase-averaged X-ray spectra and energy-resolved pulse profiles for the *Suzaku* observations and interpret them in terms of a simple model based on the reprocessing of hard X-rays by the precessing accretion disk. In Section 2, we describe the observations, and in Section 3 we present our analysis and results. In Section 4, we discuss the implications of our results and future work. All quoted uncertainties are 90% confidence for a single interesting parameter.

2. OBSERVATIONS AND DATA REDUCTION

2.1. *Suzaku*

Suzaku is an X-ray observatory launched in 2005 (Mitsuda et al. 2007), covering the 0.2–600 keV energy range with two sets of instruments: X-ray CCDs (X-ray Imaging Spectrometer: XIS) covering 0.2–12 keV and the Hard X-ray Detector (HXD), a photon-counting (non-imaging) detector covering 10–600 keV. The HXD is comprised of two instruments, the PIN (sensitive to energies 10–70 keV) and GSO (sensitive to 40–600 keV). Here, our analysis focuses on XIS observations in the 0.5–10 keV band and the PIN in the 10–50 keV band. We do not make use of GSO data as the signal in the GSO is very weak ($\lesssim 1\%$ of background). Our analysis uses XIS and PIN event files that have been reprocessed with the FTOOL `aepipeline` using the latest *Suzaku* calibration (version 2.2.7.18) and screened using the standard criteria.

Suzaku performed three observations of LMC X-4 during the high state of the superorbital cycle, when the source is bright enough to obtain a high signal-to-noise ratio. Details of the observations are shown in Table 1. These observations were carried out at the "XIS nominal" pointing position for effective exposures of $\sim$20 ks. Table 1 also gives the approximate orbital phases covered by the observations, estimated from the ephemeris of Levine et al. (2000). The exposures all avoid orbital phases close to eclipse (the range of $\phi_{\rm orb}$ is 0.1–0.8) and do not show any significant variations in flux other than the observed pulsations, so we do not expect any changes in absorption (from the companion star or accretion flow) within each exposure.

2.1.1. *XIS*

XIS consists of four detectors, each with 1024×1024 pixel X-ray-sensitive CCDs at the foci of each of the four X-ray Telescopes (Naik et al. 2008). However, at the time when the data were taken, only three of the XIS detectors (XIS0, XIS1, and XIS3) worked normally. Of these, XIS0 and XIS3 are front-illuminated (FI) chips, while XIS1 is a back-illuminated chip. XIS1 has a significantly different spectral response from the FI chips, with greater sensitivity at energies below $\sim$1.5 keV and poorer sensitivity above $\sim$ 3 keV. All XIS chips have an energy resolution $\sim$ 130 eV (FWHM) at 6 keV (Mitsuda et al. 2007). The XIS was operated with the "1/8 Window" option, which gave a time resolution of 1 s, covering a field of view of $17'.8 \times 2'.2$.

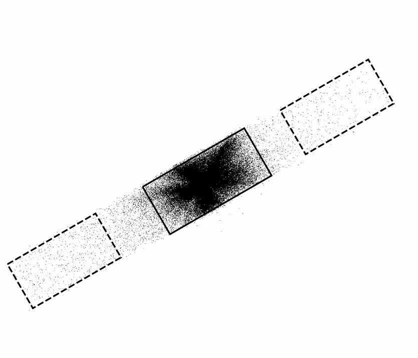

FIG. 2.— Source and background regions for analysis of *Suzaku* observations of LMC X-4. This image shows chip XI0 for observation 1. To subtract background, we extracted spectra from the source region (solid) and background regions (dashed).

We used ds9 V5.6.3, an astronomical imaging and data visualization application developed by SAO, XSELECT V2.4a, and XSPEC V12.6.0 for data analysis. We used XSELECT to combine XIS exposures taken in 3×3 and 5×5 event modes to make single event files. Next, we defined the regions for the source and the background for each observation, as shown in Figure 2. The source region was a rectangle of size $300'' \times 140''$, centered on the source and tilted 30° (for XIS0 and XIS3) and 119° (for XIS1). Background events were extracted from two rectangles of size $260'' \times 130''$ on either side of the source and aligned with the source region. We note that the XIS background is extremely low, so that background contributes only $\approx$0.5% of the total 0.5–10 keV flux from the source.

For spectral analysis, we filtered the XIS events using a good time interval (GTI) created by merging GTIs for the cleaned XIS and PIN event files as well as the PIN background event file (described in Section 2.1.2). The merged clean exposures range from $\approx$18 to 21 ks (Table 1). Using the filtered XIS event files, we extracted spectra from the source and background regions and grouped the spectra so that the total number of events in each energy interval was roughly equal. The energy bands below 2.5 keV, 2.5–7 keV, and above 7 keV are grouped by factors of 8, 16, and 32, respectively. Each (ungrouped) channel has a width of 3.65 eV.

We used the tools `xisrmfgen` and `xissimarfgen` available in the HEASOFT version 6.9 to generate XIS redistribution matrix files and ancillary response files. Following the recommendations in the *Suzaku* ABC guide[4], we generated 400,000 simulated photons in creating each ancillary response. For each observation, we combined the data from the two FI chips (XIS0 and XIS3) into a single spectrum.

We note that "wobble" of the *Suzaku* spacecraft, owing to time-dependent thermal distortions of its chassis, can cause the pointing position to vary by as much as $\sim 40''$. As this is a

---

[5] *Suzaku* ABC guide, v. 2, Section 6.6.4; JX-ISAS-SUZAKU-MEMO-2007-04.

TABLE 1
Suzaku OBSERVATIONS

Obs	ObsID	Start Date	$\phi_{\rm orb}$ [a]	Clean Exposure (ks) [b] XIS	PIN	Merge [c]
1	702038010	2008 Jan 15 08:39:26	0.46–0.78	21.7	22.9	20.5
2	702037010	2008 Feb 11 00:42:25	0.42–0.80	23.4	20.0	17.9
3	702036020	2008 Apr 5 13:15:26	0.11–0.64	25.3	24.5	21.4

[a] Based on the orbital ephemeris of Levine et al. (2000).
[b] Note that because of gaps in the exposures, the clean exposure times are roughly half the total duration of each observation as indicated by the range of orbital phases.
[c] Total good exposure time used for spectral analysis, obtained by merging the good time intervals of the XIS, PIN, and PIN background event files.

significant fraction of the size of the 1/8 Window (our extraction regions are 140″ wide), wobble may cause source flux to be lost outside the window during the XIS exposures. We examine the thermal wobble by deriving the centroid position of the source in detector coordinates (`DETX` and `DETY` in the event files) in bins of size 50 s. For $>$ 97% of the total exposure time the thermal wobble is $<$20″, for which there is negligible flux loss. Observation 3 has a brief period ($<$2 ks) of wobble $>$30″. We derive a rough estimate of the flux lost outside the window during these periods, by calculating the observed source counts after shifting the extraction region by an amount and direction corresponding to the observed thermal wobble. At most only 15% of the flux is lost outside the window at any given time, and the total flux lost over the full observation is $<$1.5%. We thus verify that losses due to thermal wobble are minimal, and for simplicity we do not exclude the brief intervals of large wobble from the analysis.

2.1.2. *PIN*

We include PIN data in the spectral and timing analysis. As the HXD is a non-imaging instrument, we cannot estimate background directly from the observations. The PIN background consists of an instrumental component as well as the cosmic X-ray background (CXB). The instrumental background is estimated using the version 2 “tuned” background event files[7]. Spectra were extracted for both the observations and the background file and corrected for dead time. As with the XIS, spectra were extracted using the merged GTI described above. The CXB component is modeled during spectral analysis, as a power law with a high-energy exponential cutoff[9]; this component is only $\sim$2% of the observed flux.

2.2. *RXTE*

RXTE was launched on 1995 December 30 (Swank 2006). The *RXTE* ASM observes bright X-ray sources in the range of 1.5 – 12 keV, to explore the variability of sources including black holes, neutron stars, X-ray pulsars, and bursts of X-rays. ASM scans about 80% of the sky every orbit, allowing monitoring on timescales of 90 minutes or longer. Details about the *RXTE* ASM can be found in Levine et al. (1996). In this paper, we use 13 years of the *RXTE* ASM data on LMC X-4 from 1996 to 2009. We retrieve the one-day average light curve from the public MIT Web site[11].

3. DATA ANALYSIS AND RESULTS

3.1. *Superorbital Period Determination*

In order to determine the superorbital period during the time of our Suzaku observations, we first apply an epoch folding method to the 13 years of *RXTE* data to obtain an updated superorbital period. By comparing the variance of the folded light curve with the variance within each bin (the ANOVA method; Davies 1990, 1991), we calculate the Davies L statistic for different superorbital periods. Gaussian fits to the period versus L statistic, for different numbers of phase bins, all give about 30.316 days at high significance. A power spectrum using the Lomb Normalized Periodogram (Scargle 1982) is also consistent with 30.32 days. This result is consistent with the superorbital period determined using five years of *RXTE* data by Paul & Kitamoto (2002). This suggests no significant change in the long-term period over the 13 years of *RXTE* observations, in contrast to the results of Paul & Kitamoto (2002) who had found a long-term decrease in the period over the preceding 20 years. We estimate the error by re-folding the light curve into various numbers of bins and examining the resulting best fit. Both the ANOVA and Lomb Normalized Periodogram methods determine a long-term period of 30.32 ± 0.04 days. Figure 3 shows a plot of our best-fit period superposed on the 13 year *RXTE* ASM light curve. A study was made of possible variability in the long-term period over the *RXTE* ASM lifetime and the folded light curve gave similar results near the times of the *Suzaku* observations as the steady period model.

We note that the L statistic does not make use of uncertainties in the *RXTE* lightcurve. As a check, we performed an *e*-folding analysis using the FTOOL `efsearch` to derive the period that maximizes χ^2 relative to no variation. We used 8, 16, or 32 phase bins with time resolutions of 0.09, 0.05, or 0.02 days, respectively. We obtained long-term periods of 30.29 ± 0.09, 30.29 ± 0.05, and 30.32 ± 0.02 (where the errors are the period resolutions of the search), corresponding to maximum χ^2 of 890, 959, and 1070, respectively. These estimates are consistent with our result derived from the ANOVA and Lomb Normalized Periodogram methods.

Our improved fit to the superorbital period allows us to accurately determine the phases of our *Suzaku* observations as shown in Figure 4. We define the start of the high state of the superorbital cycle (ϕ_{30} = 0) to be at JD 2454560.0.

3.2. *Phase-averaged Spectroscopy*

For each observation, we perform spectroscopic fits to the XIS FI, XIS 1, and PIN spectra simultaneously, for a combined spectral range of 0.6–50 keV. We fit all three spectra with the same spectral model, but allow the overall normalizations to vary in order to allow for uncertainties or systematic offsets in the flux calibration. Fits to the power-law spectrum

---

[6] JX-ISAS-SUZAKU-MEMO-2007-04
[8] ftp://legacy.gsfc.nasa.gov/suzaku/data/background/pinnxb_ver2.0/
[10] *Suzaku* ABC guide, v. 2, Section 7.3.3.1
[12] http://xte.mit.edu/ASM_lc.html

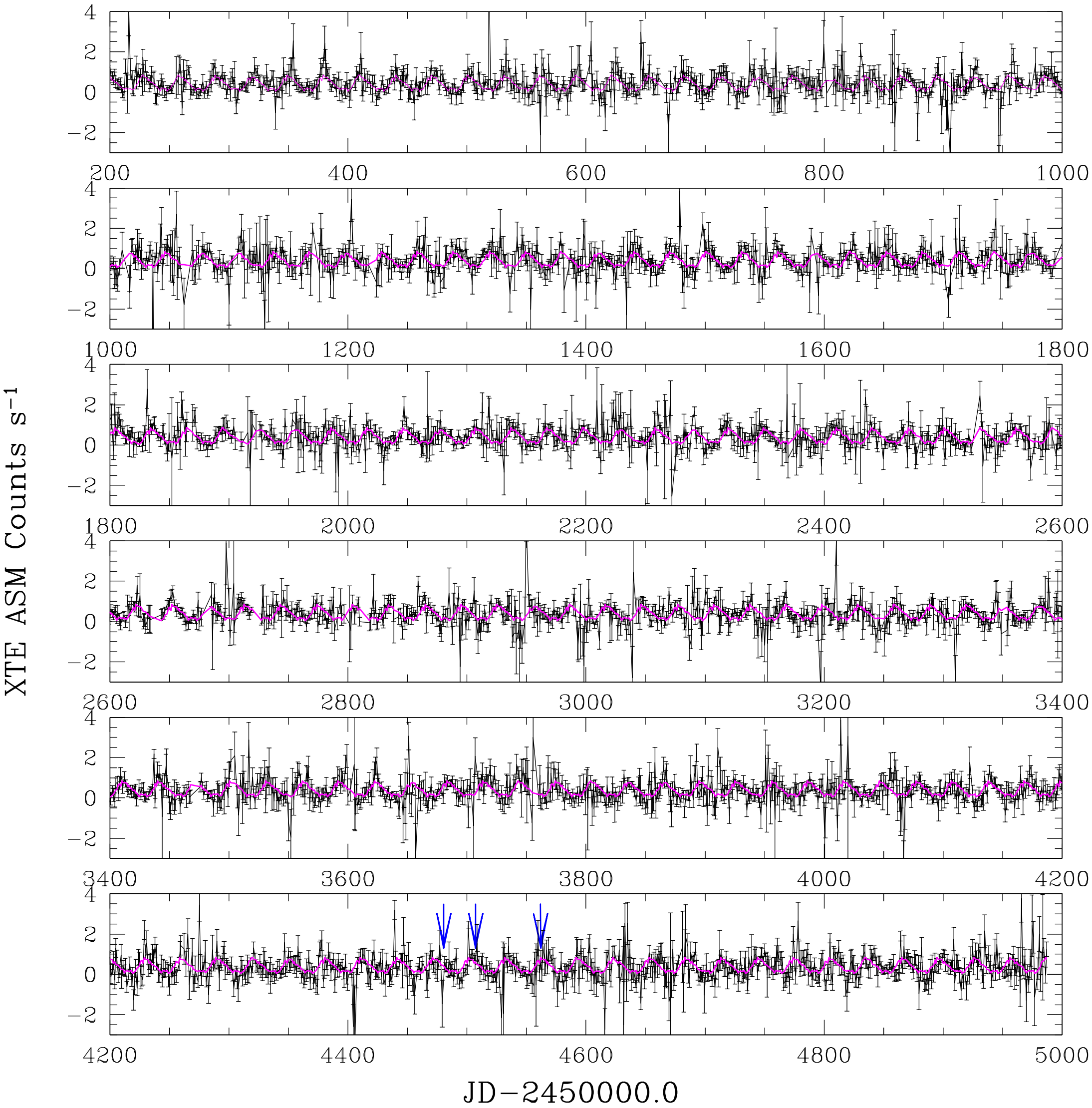

FIG. 3.— One-day average light curve of LMC X-4 covering 13 years of observations (1996 – 2009) by the *RXTE* ASM. The magenta line is our best fit to the 30.32 ± 0.04 days superorbital period of LMC X-4. The hats on the error bars denote the widths of the time over which the data were averaged (1 day for the ASM data).

of the Crab nebula indicate that the best-fit normalizations for the three XIS chips are consistent to within a few percent, while the best-fit normalization for the PIN relative to XIS is 1.16[13].

We first fit the phase-averaged spectra with a simple continuum model of power-law plus blackbody that has previously been successfully employed for LMC X-4 (Paul et al. 2002), as well as a number of other X-ray pulsars (Hickox et al. 2004). Previous studies have found evidence for a high-energy cutoff in the power-law component; La Barbera et al. (2001) use a cutoff of the form

$$e^{(E-E_{\rm cut})/E_{\rm fold}}; E \geq E_{\rm cut} \qquad (1)$$

with $E_{\rm cut} \approx E_{\rm fold} \approx 18$ keV. We find that for the *Suzaku* data the spectra are better described by a Fermi-Dirac cutoff (e.g., Coburn et al. 2002; Rivers et al. 2010) of the form:

$$1/(1+e^{(E-E_{\rm cut})/E_{\rm fold}}), \qquad (2)$$

with $E_{\rm cut} \approx 27$ keV and $E_{\rm fold} \approx 8$ keV.

In the XIS data, we exclude the energy range 1.5–3 keV to avoid instrumental effects near the Au and Si edges (Miller et al. 2008; Saez et al. 2009). We include neutral hydrogen absorption fixed to the Galactic value of $N_{\rm H} = 0.057 \times 10^{22}$ cm^{-2} (Paul et al. 2002). Our best-fit parameters for this simple model give a blackbody with $kT_{\rm BB} \sim 0.18$ keV and a power law with photon index $\Gamma \sim 0.6$, similar to results from previous studies (Paul et al. 2002; La Barbera et al. 2001). Spectral fits are shown in Figure 5, and fit parameters are given in Table 2.

A single cutoff power law provides a reasonable fit to the high-energy component in the full range from 1 to 50 keV; the best-fit photon index for the joint XIS and PIN analysis is consistent (within 2%) from that derived from fitting the XIS data alone. We note that Figure 5 shows a departure from the

[14] JX-ISAS-SUZAKU-MEMO-2008-06

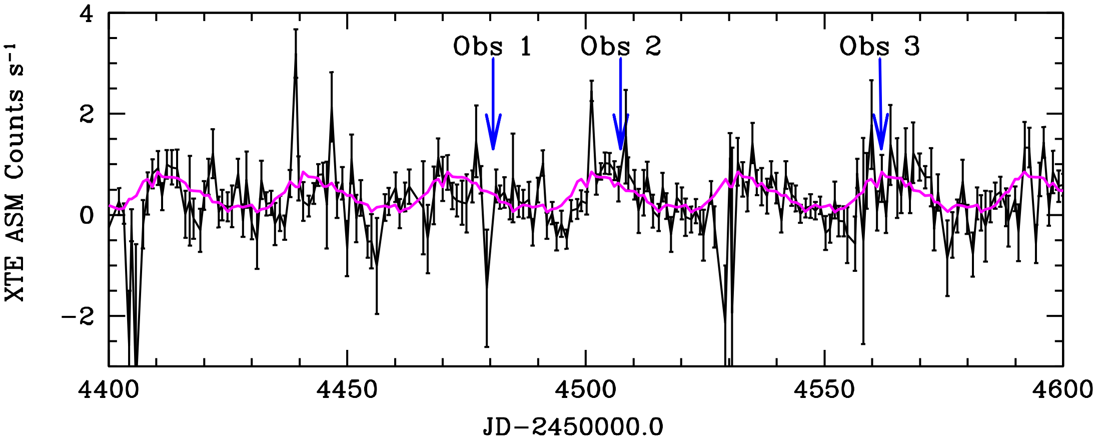

FIG. 4.— Close up of ASM count and the region of the *Suzaku* observations. Blue arrows indicate the times of our *Suzaku* observations. The superorbital phases for the three observations (left to right) are $\phi_{30} = 0.39$, $\phi_{30} = 0.27$, and $\phi_{30} = 0.07$. The zero superorbital phase is defined as the beginning of a high state (JD 2454560.0). The magenta line is our best fit of the superorbital period of LMC X-4. The hats on the error bars denote the widths of the time over which the data were averaged (1 day for the ASM data). The widths of the arrows denote the length of our observations (about 20ks each).

cutoff power law at $\sim$40 keV for observation 1. This feature does not appear in observations 2 and 3, and so for simplicity we model all three observations with the simple cutoff power law.

In the XIS spectrum at $E < 10$ keV, it is clear from the residuals in Figure 5 that other, line-like spectral features are present in addition to the simple continuum model. Emission line features are often observed in X-ray binaries; for example, in SMC X-1, several emission lines from O, Ne, Mg, Si, S, Ar, and Fe were needed to fit the spectrum (Vrtilek et al. 2005). In addition, using the *Chandra* High-Energy Transmission Grating Spectrometer and the *XMM-Newton* Reflection Grating Spectrometer, Neilsen et al. (2009) performed X-ray spectroscopy of LMC X-4 and detected several X-ray emission lines. In the *Suzaku* observations, we find at least four emission lines including O VIII, Ne IX (X Ly$_\alpha$), Fe K$_\alpha$, and broad Fe (line energies and equivalent widths (EWs) are given in Table 3). The total χ^2 values for every observation are lower by at least 30 when adding each individual emission line. Following Avni (1976) and Yaqoob (1998), we are $>$90% confident that the line features are detected. The average χ^2 per degree of freedom for the three observations is reduced from 2.5 to 1.2. The spectral fits are shown in Figure 6, and the results are listed in Table 4.

We note that for observations 1 and 3, with the inclusion of emission lines, the best-fit relative normalizations between the PIN and the XIS FI spectra are broadly consistent with the value of 1.16 derived from calibration studies and higher than the value of $\approx$1.07 for the pure continuum model.

As an alternative to blackbody model for the soft component, we also consider models for optically thin thermal emission, which have previously been used to describe the soft emission from LMC X-4 (Paul et al. 2002; Naik & Paul 2004). We consider both a thermal bremsstrahlung model and an optically thin (MEKAL) model that includes contributions from metal lines (e.g., Haberl & Pietsch 2005). We perform fits using a model identical to that described above including emission lines, but replacing the blackbody component with the thermal bremsstrahlung and MEKAL models. We find that these can represent the soft component equally well to the blackbody model (although the MEKAL model requires very low metallicity $<$ 2% of solar). Therefore, we cannot rule out these models for the soft excess on spectral grounds. However, we can rule them out on physical grounds, following the argument of (Hickox et al. 2004). It is possible that the diffuse cloud of gas around the neutron star (Boroson et al. 2001) would reprocess the hard X-ray and produce optically thin emission that might be described by optically thin emission models. However, in order to produce high $L_{\rm soft}$ as observed in LMC X-4, the system must have the emission region $R_{\rm cloud} > 10^{12}$ cm, which is larger than the size of the emission region $R_{\rm cloud} \lesssim 10^{11}$ cm as inferred from the decrease in soft flux during the eclipse. Further, such a large region cannot produce soft pulsations as observed. Therefore, although the optically thin models provide an adequate description of the data, we prefer the blackbody model for our physical interpretation of the soft component.

For all the spectral fits shown in Figs. 5 and 6, the blackbody component dominates the energy range below 1 keV, while power-law emission dominates above 2 keV. We propose that the hard (power-law) X-rays from the pulsar are reprocessed by the inner accretion disk, where the soft pulses are emitted. The power-law flux is $(8\text{–}10) \times 10^{-9}$ erg cm^{-2} s^{-1}, assuming the absolute flux calibration of the XIS FI chips. Taking the distance to LMC to be 50 kpc, we obtain $L_X \sim 3 \times 10^{38}$ erg s^{-1} from 2 to 50 keV. The bolometric luminosity of the blackbody component (taken directly from the XSPEC normalization) is $\sim 1.5 \times 10^{37}$ erg s^{-1}.

Using the observed temperatures and luminosities, we can derive the size of the blackbody-emitting region, assuming that the emission is from a spherical region that partially covers the central source. Note that this differs from another commonly used estimate for the blackbody radius, which assumes a circular emission geometry. We prefer the spherical partial covering geometry, because for this source the blackbody emission is likely due to the reprocessing of the hard emission from the neutron star (Hickox et al. 2004). For a partial covering spherical shell and an incident hard X-ray luminosity L_X, the radius of the shell (as shown in Figure 9 of Hickox et al. 2004) is

$$R_{\rm BB}^2 = \frac{L_X}{4\pi\sigma T_{\rm BB}^4}. \qquad (3)$$

TABLE 2
FITS USING A POWER LAW AND A BLACKBODY TO *Suzaku* OBSERVATIONS

Parameter	Observation 1	Observation 2	Observation 3
χ^2_ν (317 dof)	2.90	2.53	2.18
N_H ($\times 10^{22}$ cm^{-2}) (fixed)	5.7×10^{-2}	5.7×10^{-2}	5.7×10^{-2}
Continuum			
kT_BB (keV)	0.181 ± 0.002	0.174 ± 0.002	0.181 ± 0.002
N_BB[a]	$(6.32^{+0.09}_{-0.08}) \times 10^{-4}$	$(6.99 \pm 0.11) \times 10^{-4}$	$(5.57^{+0.09}_{-0.11}) \times 10^{-4}$
Power-law Γ	0.56 ± 0.02	0.56 ± 0.02	0.56 ± 0.02
N_Γ[b]	$(0.67 \pm 0.02) \times 10^{-2}$	$(1.05 \pm 0.03) \times 10^{-2}$	$(0.83 \pm 0.02) \times 10^{-2}$
E_cut (keV)	$25.3^{+1.0}_{-1.2}$	$24.8^{+1.3}_{-1.6}$	$24.7^{+1.2}_{-1.5}$
E_fold (keV)	$7.1^{+0.6}_{-0.5}$	8.6 ± 0.6	8.1 ± 0.6
Relative Normalizations			
A_XIS1	1.01 ± 0.01	0.95 ± 0.01	1.02 ± 0.01
A_PIN	1.07 ± 0.03	1.05 ± 0.03	1.09 ± 0.03

[a] XSPEC normalization, units of 8.36×10^{-8} erg cm^{-2} s^{-1} (bolometric).
[b] XSPEC normalization, units of photons cm^{-2} s^{-1} at 1 keV.

TABLE 3
X-RAY EMISSION LINES USED IN FITTING SPECTRA OF LMC X-4

Line	Wavelength (Å)	Line Energy (keV)	Observed Energy (keV)[a]	Equivalent Width (eV) [b]
O VIII Ly$_\alpha$	18.97	0.65	0.60–0.62	41 ± 13
Ne IX (Ne X Ly$_\alpha$)	13.45 (12.13)	0.91 (1.02)	0.98–0.99	13 ± 5
Fe K$_\alpha$	1.94	6.38	6.40–6.51	25 ± 19
Broad Fe	1.89	· · ·	6.52–6.61	150 ± 50

[a] Range of best-fit line energies for the three observations.
[b] Average EWs and uncertainties between the three observations.

Using $L_X \sim 3 \times 10^{38}$ erg s^{-1} and $kT_\mathrm{BB} \sim 0.18$ keV, we have $R_\mathrm{BB} \sim 1.5 \times 10^8$ cm. In this picture, the covering fraction Ω of the spherical shell is given by simply $\Omega = L_\mathrm{BB}/L_X$ and so is relatively small ($\Omega \sim 0.05$).

In LMC X-4, an estimate for the magnetic field comes from the observed cyclotron feature at $\sim$ 100 keV (La Barbera et al. 2001). We note that the existence of this feature has been a matter of debate (e.g., Tsygankov & Lutovinov 2005), but since it provides the only existing estimate for the magnetic field in this source, we adopt it in the subsequent analysis. A cyclotron energy of 100 keV would indicate $B \sim 10^{13}$ G. An estimate of the magnetospheric radius (e.g., Ghosh & Lamb 1979; Frank et al. 2002) is

$$R_\mathrm{m} \sim 0.5 R_\mathrm{A} \sim 1.5 \times 10^8 m_1^{1/7} R_6^{10/7} L_{37}^{-2/7} B_{12}^{4/7} \mathrm{cm}, \qquad (4)$$

where R_A is the standard Alfvén radius. Here, m_1 is the mass of the neutron star in $M_\odot$, R_6 is its radius in 10^6 cm, L_{37} is the X-ray luminosity in 10^{37} erg s^{-1}, and B_{12} is the neutron star surface magnetic field in 10^{12} G. Assuming $m_1 = 1.25$, $R_6 \sim 1$, $L_{37} = 30$, and $B_{12} \sim 10$, we obtain $R_m \sim 2 \times 10^8$ cm and $R_\mathrm{BB}/R_m \sim 0.7$.

We note that if we evaluate L_X only in the range 0.5–10 keV, we obtain $L_X \sim 1 \times 10^{38}$ erg s^{-1} and $R_\mathrm{BB} \sim 9 \times 10^7$ cm, similar to results obtained by ASCA in the same energy range (Paul et al. 2002); this highlights the need to consider higher energies where the bulk of the hard component is emitted.

3.3. *Timing Analysis*

Our pulse-phase-averaged spectral analysis suggests that the soft and hard spectral components for LMC X-4 have different physical origins (as discussed in detail by Hickox et al. 2004). We examine the time variation of these components separately, by deriving energy-resolved pulse profiles at the different superorbital phases. We derive pulse periods from the PIN observations, which have time resolution of 61 μs. We are also able to study pulsations with XIS, which in 1/8 Window mode has time resolution (1 s) that is sufficient to produce pulse profiles for LMC X-4's 13.5 s period (the XIS event arrival times were randomized within the 1 s time bins). Any variations in source flux on timescales longer than the pulse period should not significantly affect the derived pulse profiles. Therefore, to maximize signal to noise in the timing analysis, we used the full clean GTIs for each detector (unlike for the spectral analysis, for which we filtered the XIS and PIN data with a common GTI).

We corrected both the PIN and XIS events to the rest frame of the solar system using the `aebarycen` tool and corrected for the orbital motion of the LMC X-4 system using the ephemeris of Levine et al. (2000). Using the FTOOL `efsearch`, we derived pulse periods for the PIN data by searching for the maximum in the χ^2 versus folding period. We obtain $P_\mathrm{pulse} = 13.5087 \pm 0.0002$ s, 13.5091 ± 0.0001 s, and 13.5096 ± 0.0001 s for observations 1–3, respectively. Uncertainties are estimated both from formal errors on the fit to the χ^2 versus period and also by a jackknife resampling technique, calculating the period after excluding successive $\sim$4 ks GTIs; these two estimates give consistent uncertainties. The drift in P_pulse over the three months between observations 1 and 3 is consistent with typical rates of spin evolution observed previously for LMC X-4 (e.g., Woo et al. 1996; Levine et al. 2000).

TABLE 4
FITS INCLUDING EMISSION LINES TO *Suzaku* OBSERVATIONS

Parameter	Observation 1	Observation 2	Observation 3
χ^2_ν (308 dof)	1.27	1.20	1.08
$N_{\rm H}$ ($\times 10^{22}$ cm^{-2}) (fixed)	5.7×10^{-2}	5.7×10^{-2}	5.7×10^{-2}
Continuum			
$kT_{\rm BB}$ (keV)	$0.183^{+0.003}_{-0.002}$	0.174 ± 0.003	0.183 ± 0.003
$N_{\rm BB}$[a]	$(5.69^{+0.12}_{-0.13}) \times 10^{-4}$	$(6.24^{+0.16}_{-0.13}) \times 10^{-4}$	$(5.05 \pm 0.12) \times 10^{-4}$
Power-law Γ	0.64 ± 0.02	0.63 ± 0.02	0.62 ± 0.02
N_Γ[b]	$(0.73 \pm 0.02) \times 10^{-2}$	$(1.12 \pm 0.03) \times 10^{-2}$	$(0.88^{+0.03}_{-0.02}) \times 10^{-2}$
$E_{\rm cut}$ (keV)	$26.7^{+0.9}_{-1.0}$	$26.5^{+1.2}_{-1.3}$	$26.1^{+1.1}_{-1.3}$
$E_{\rm fold}$ (keV)	$6.8^{+0.6}_{-0.5}$	8.3 ± 0.6	7.9 ± 0.6
Emission Lines			
$E_{\rm O}$ (keV)	0.62 ± 0.02	0.60 ± 0.02	0.61 ± 0.02
$\sigma_{\rm O}$ (keV)	5.0×10^{-2}	5.0×10^{-2}	5.0×10^{-2}
$I_{\rm O}$ (photons cm^{-2} s^{-1})	$(2.5^{+0.7}_{-0.5}) \times 10^{-3}$	$(3.4^{+1.6}_{-0.8}) \times 10^{-3}$	$(2.5^{+0.7}_{-0.6}) \times 10^{-3}$
$E_{\rm Ne}$ (keV)	0.98 ± 0.02	$0.99^{+0.02}_{-0.01}$	0.98 ± 0.03
$\sigma_{\rm Ne}$ (keV)	5.0×10^{-2}	5.0×10^{-2}	5.0×10^{-2}
$I_{\rm Ne}$ (photons cm^{-2} s^{-1})	$(3.8^{+0.8}_{-0.7}) \times 10^{-4}$	$(4.7^{+0.8}_{-0.9}) \times 10^{-4}$	$(2.4 \pm 0.7) \times 10^{-4}$
$E_{\rm Fe}$ (keV) first Gaussian	6.41 ± 0.03	6.40 ± 0.04	$6.51^{+0.06}_{-0.05}$
$\sigma_{\rm Fe}$ (keV)	5.0×10^{-2}	5.0×10^{-2}	5.0×10^{-2}
$I_{\rm Fe}$ (photons cm^{-2} s^{-1})	$(7.0^{+2.6}_{-2.7}) \times 10^{-5}$	$(7.9^{+3.0}_{-3.2}) \times 10^{-5}$	$(6.5^{+2.3}_{-2.4}) \times 10^{-5}$
$E_{\rm Fe}$ (keV) second Gaussian	$6.53^{+0.06}_{-0.05}$	$6.61^{+0.07}_{-0.06}$	6.52 ± 0.09
$\sigma_{\rm Fe}$ (keV)	$0.37^{+0.08}_{-0.07}$	$0.37^{+0.09}_{-0.07}$	$0.53^{+0.15}_{-0.14}$
$I_{\rm Fe}$ (photons cm^{-2} s^{-1})	$(3.7^{+0.6}_{-0.5}) \times 10^{-4}$	$(4.5^{+0.9}_{-0.8}) \times 10^{-4}$	$(3.7^{+0.5}_{-0.8}) \times 10^{-4}$
Relative Normalizations			
$A_{\rm XIS1}$	1.01 ± 0.01	0.95 ± 0.01	1.01 ± 0.01
$A_{\rm PIN}$	$1.15^{+0.04}_{-0.03}$	1.12 ± 0.03	1.15 ± 0.03

[a] XSPEC normalization, units of 8.36×10^{-8} erg cm^{-2} s^{-1} (bolometric).

[b] XSPEC normalization, units of photons cm^{-2} s^{-1} at 1 keV.

As a check, we derived pulse periods from the XIS data, using the combined event file for the XIS0, XIS1, and XIS3. We obtain similar pulse periods of $P_{\rm pulse} = 13.5089 \pm 0.0001$ s, 13.5095 ± 0.0001 s, and 13.5100 ± 0.0003 s; the resulting pulse profiles are qualitatively identical if we use these periods rather than those from the PIN.

We note that we have not accounted for any deviation from orbital ephemeris derived by Levine et al. (2000), which could possibly affect the derived spin periods. However, the relative pulse profiles in the different X-ray bands, which are the focus of this study, will be largely independent of the exact absolute spin period. We leave a detailed analysis of the spin evolution of LMC X-4 to a future study.

Using the above spin periods, we created separate pulse profiles for the XIS in the 0.5–1 keV ("soft") band (which is dominated by the soft blackbody spectral component) and the 2–10 keV ("medium") band (which is dominated by the hard power-law component). We also derived profiles for the PIN in the 10–50 keV ("hard") band that is entirely dominated by the hard (cutoff) power law. We have subtracted the background flux in producing the PIN pulse profiles (the XIS background is negligible).

The pulse profiles are shown in Figures 7–9 and show significant differences in the pulse profile for the different X-ray energies. The soft and hard pulses in all three observations are broad and show single peaks, while observations 2 and 3 show double-peaked profiles in the medium band, similar to those observed in Her X-1 (Zane et al. 2004) and SMC X-1 (Neilsen et al. 2004; Hickox & Vrtilek 2005), although the pulsations for observation 3 are relatively weak. In contrast observation 1 shows only a single peak in the medium pulse profile, similar to the observed soft pulses. The variations between the hard and medium pulses indicate that the spectral shape of the medium component may change with pulse phase and further that these variations may differ between observations.

In addition, the phase shifts between pulses at different energies vary among the observations. In observation 1, all three pulses are almost in phase with each other, while observations 2 and 3 show notable phase shift. We study this phase shift in more detail by cross-correlating the soft profiles against the hard and medium profiles (see Figure 10). We first examine the cross-correlation between soft (0.5–1 keV) and hard (10–50 keV) pulses, shown in the top panel of Figure 10. These energy bands represent the bulk of the blackbody and hard power flux, respectively. Observation 1 shows a strong positive cross-correlation between soft and hard pulses peaking at $\sim$-40°, indicating that the soft pulses slightly lag the hard pulses. The cross-correlations for observations 2 and 3 peak almost exactly out phase at $\sim$180°, although there is an indication that the observation 3 may be slightly shifted to shorter phase lag (by $\sim$10°). However, the precise relative lag is difficult to measure because the pulse profiles have relatively few (10) bins.

The cross-correlations between the medium (2–10 keV) pulses and the hard and soft pulses are shown in the bottom two panels of Figure 10. For observation 1, the cross-correlations peak near zero as the phase of the medium pulses closely aligned with the soft and hard pulses. The cross-correlations for observations 2 and 3 are more complex, be-

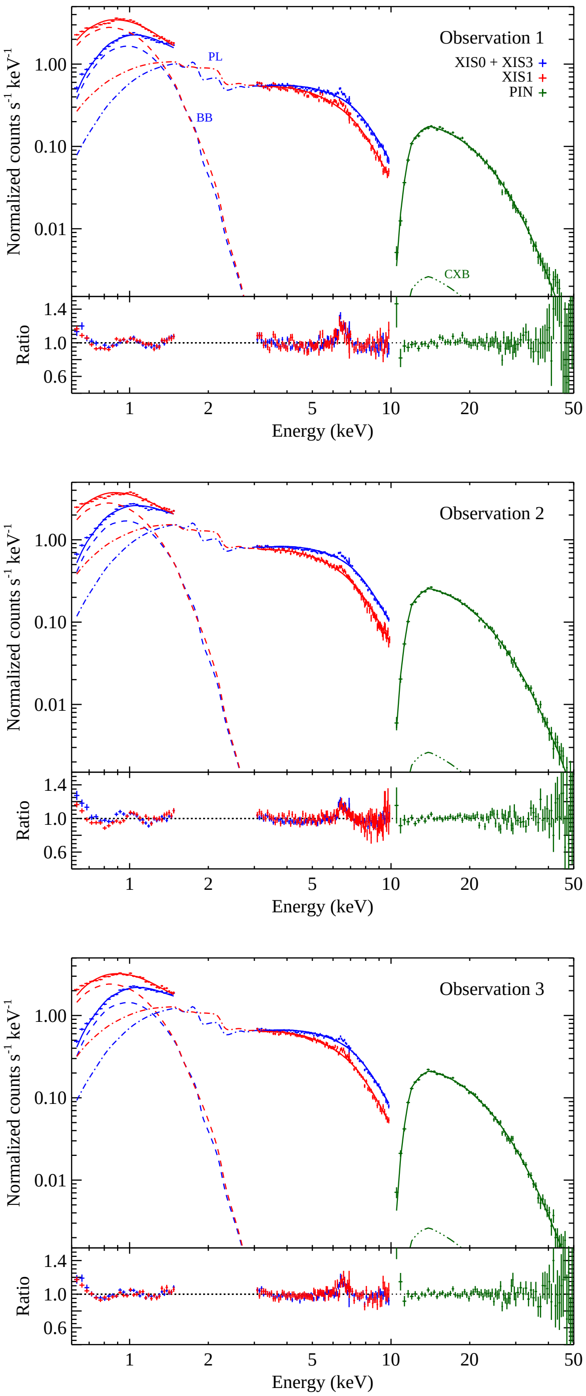

FIG. 5.— Phase-averaged *Suzaku* spectra for the three observations, fitted with a continuum consisting of a blackbody (dashed) plus power law with high-energy cutoff (dash dot). The FI, XIS1, and PIN spectra are shown in blue, red, and green, respectively. The individual spectral components are shown, including the CXB model for the PIN spectrum. Note the significant line-like residuals.

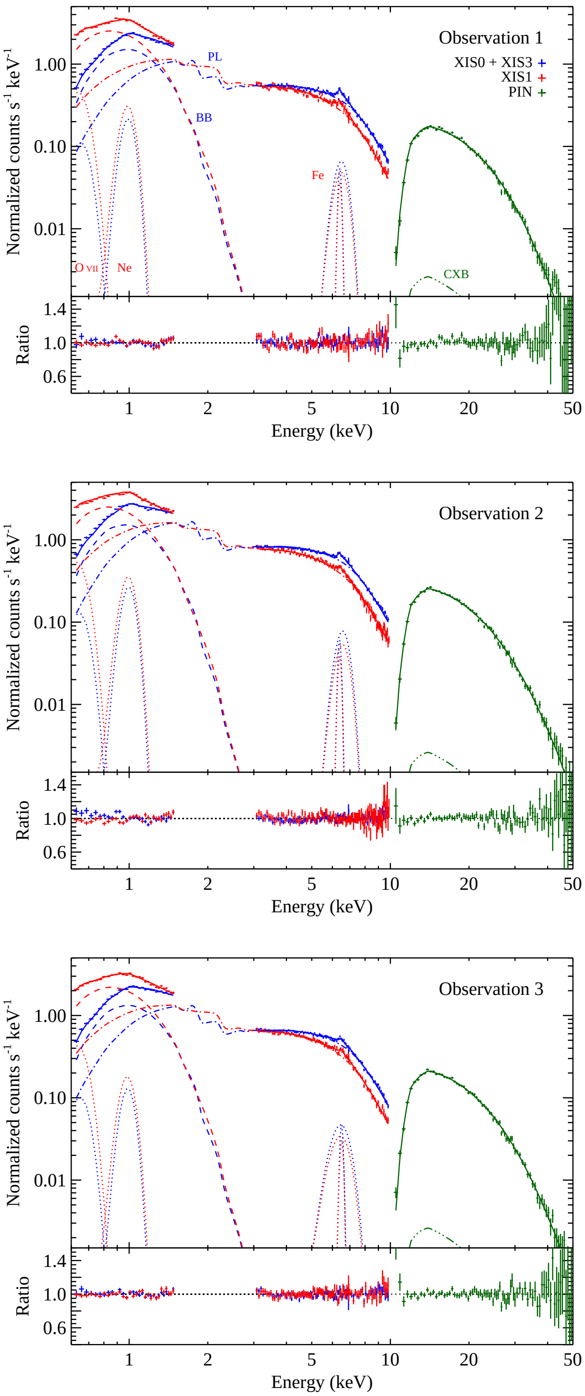

FIG. 6.— Phase-averaged spectra from *Suzaku* observations with blackbody (dashed), power law with high-energy cutoff (dash dot), and emission line (dotted) components shown. The FI, XIS1, and PIN spectra are shown in blue, red, and green, respectively. The emission lines are broad Fe, Fe K$_\alpha$, O VIII, and Ne IX (X Lyα). The inclusion of the lines significantly improves the residuals compared to the continuum fits shown in Figure 5.

cause of the multiple peaks in the medium pulse profiles. We note that the phase offset between medium and hard pulses varies more strongly than between medium and soft pulses.

4. DISCUSSION

We use 13 years of available *RXTE*/ASM data to determine a superorbital period of 30.32±0.04 days for LMC X-4. The long time series allows an improvement by a factor of 10 in precision compared to the measurement of Lang et al. (1981). Our period estimate is consistent with that of Lang et al. (1981), indicating that the period has been relatively stable over the past ∼30 years. The improved period allows us to accurately determine the superorbital phases of our *Suzaku* observations and will facilitate future studies that require accurate estimates of ϕ_{30}.

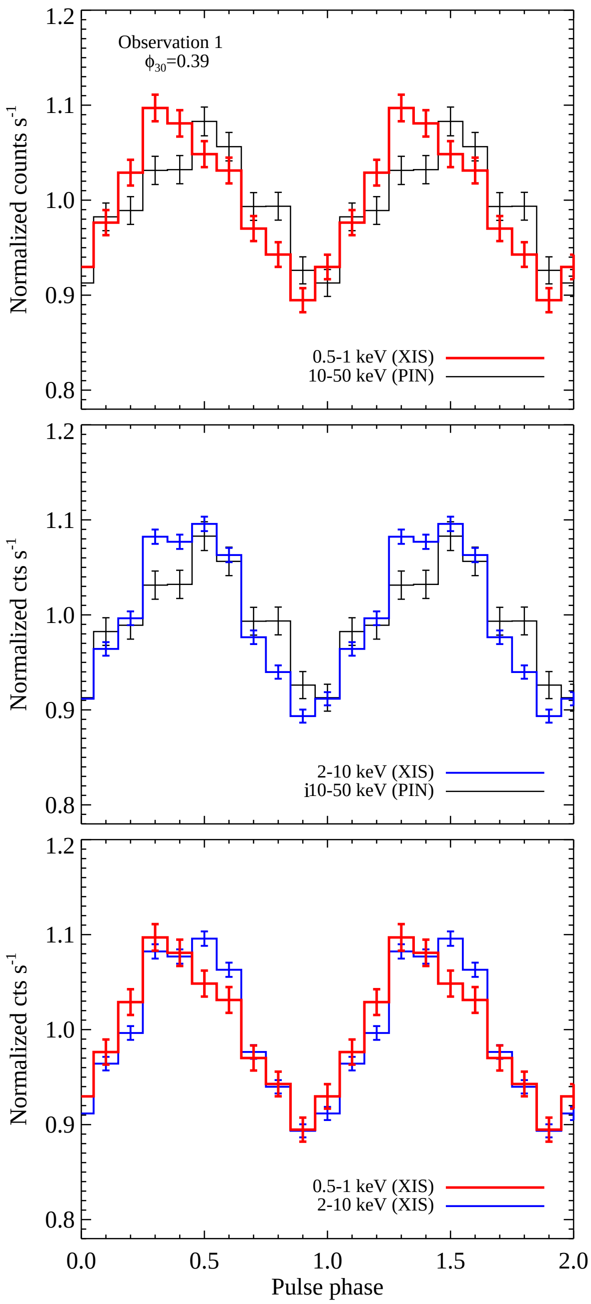

FIG. 7.— Energy-resolved pulse profiles for observation 1. The soft (0.5–1 keV, red) pulses are dominated by the blackbody component, while the medium (2–10 keV, blue) and hard (10–50 keV, black) pulses are dominated by the power law. The profiles for observations 2 and 3 are shown in Figures 8 and 9, respectively; note the variation in the medium pulse profile and the varying phase offset between the hard, medium, and soft pulses for the different superorbital phases.

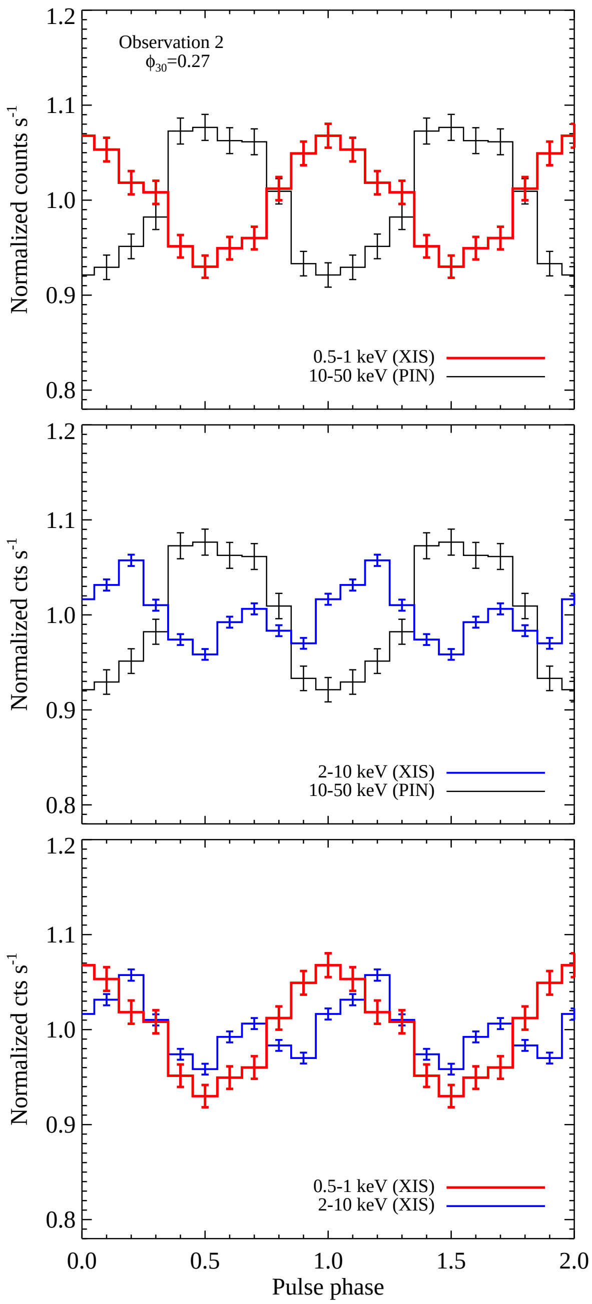

FIG. 8.— Energy-resolved pulse profiles (as in Figure 7), for observation 2.

In the *Suzaku* observations, we find that the continuum over roughly two decades in energy (0.6–50 keV) can be described by a blackbody plus a cutoff high-energy power law. In addition, we detect four emission features as listed in Table 3. (All of the four emission lines have been detected in SMC X-1; (Vrtilek et al. 2005).) Limited by the energy resolution ($\sim$ 130 eV) of XIS detectors, we cannot clearly identify the line with energy 0.98 keV. Our possible candidates are Ne IX (0.91 keV) and Ne X Ly$_\alpha$ (1.02 keV). For the Fe K$_\alpha$ line, it has been detected from many previous studies (e.g., La Barbera et al. 2001; Naik & Paul 2003, and references therein). Neilsen et al. (2009) suggested that Fe K$_\alpha$ line originates at the outer accretion disk. In addition to Fe K$_\alpha$ at 6.4 keV, we also detect a broad Fe line. Using $M = 1.25 M_\odot$ for the neutron star and $R_{\rm BB} \sim 1.5 \times 10^8$ cm, we find the velocity at the inner accretion disk to be $\sim 1.1 \times 10^4$ km s^{-1}, which corresponds to Doppler shift of 0.2 keV for Fe K$_\alpha$. This is of similar order (although somewhat smaller than) the average $\sigma \approx 0.4$ keV derived from the spectral fits. Given this rough correspondence (and the considerable uncertainties in the geometry of the accretion flow), we argue that this broad Fe line is Doppler broadened Fe K$_\alpha$ emitted from the inner

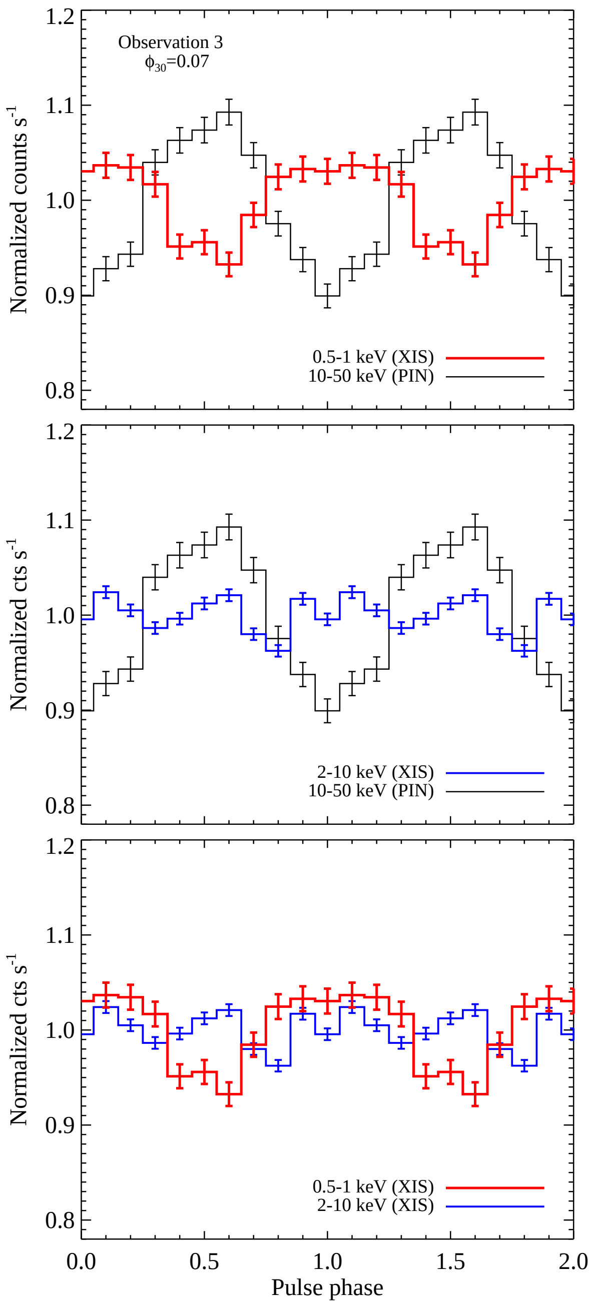

FIG. 9.— Energy-resolved pulse profiles (as in Figure 7), for observation 3.

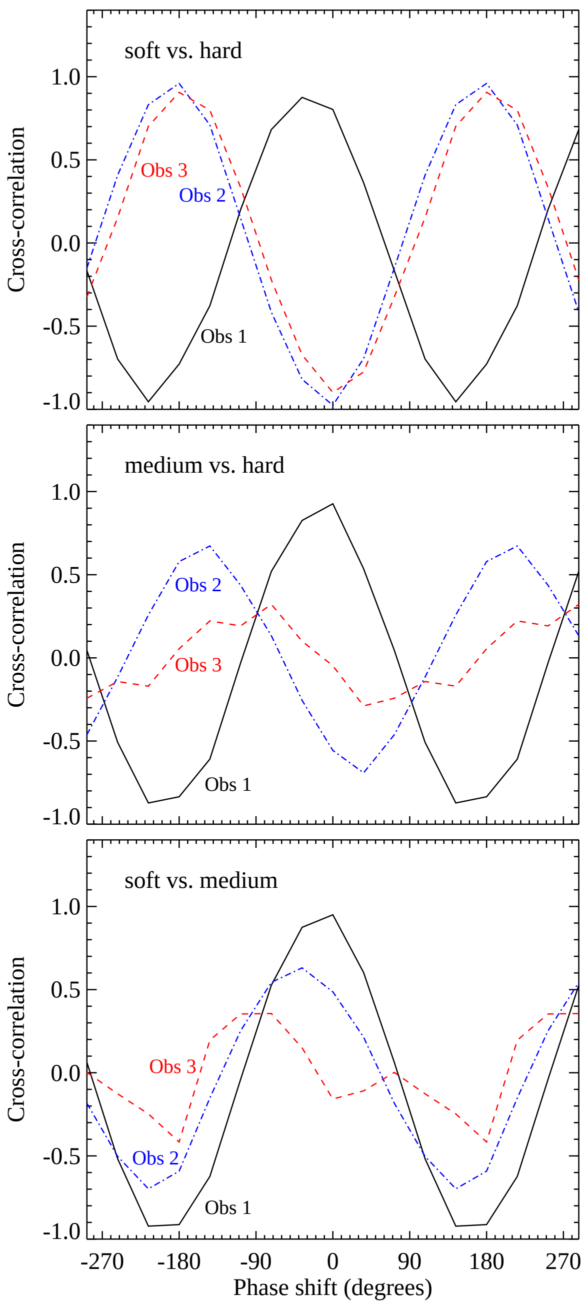

FIG. 10.— Cross-correlation between energy-resolved pulse profiles, showing the variation in relative phase and shape of the pulses for the three *Suzaku* observations. A positive phase shift corresponds to the first pulses listed leading the second pulses listed. For example, in the top panel, the peak at ∼ −40° shift for observation 1 indicates that the soft pulses lag the hard pulses by ∼40°.

accretion disk due to the high velocity, as also suggested by Neilsen et al. (2009).

It is challenging to estimate the fluorescent Fe line flux that would be expected for reprocessing by the inner disk. For the partial spherical geometry described above with $\Omega = 0.05$, a model of reflection from a neutral disk (George & Fabian 1991) predicts an Fe K line EW $\sim$ 25 eV, similar to the EW of the observed narrow line but smaller than the broad Fe feature, which has EW = 150 ± 50 eV. We note, however, that such a broad feature could be produced by emission from iron in a range of ionization states (e.g., Ramsay et al. 2002) and could also be due to complex absorption around the Fe K edge, as observed in some active galactic nuclei (e.g., Yaqoob et al. 1995) and polars (e.g., Done & Magdziarz 1998). Finally, disk reflection would predict the presence of a Compton reflection feature which we have not included in our simple power-law model for the continuum, and which might affect the observed EW. In light of these uncertainties, it is notable that a broad Fe feature with similar EW $\sim$ 150 eV has also been observed in Her X-1, for which correlations in the pulse profiles for the soft (blackbody) component and the Fe K line suggest that both originate from the inner disk (Ramsay et al. 2002; Zane et al. 2004). We conclude that inner disk repro-

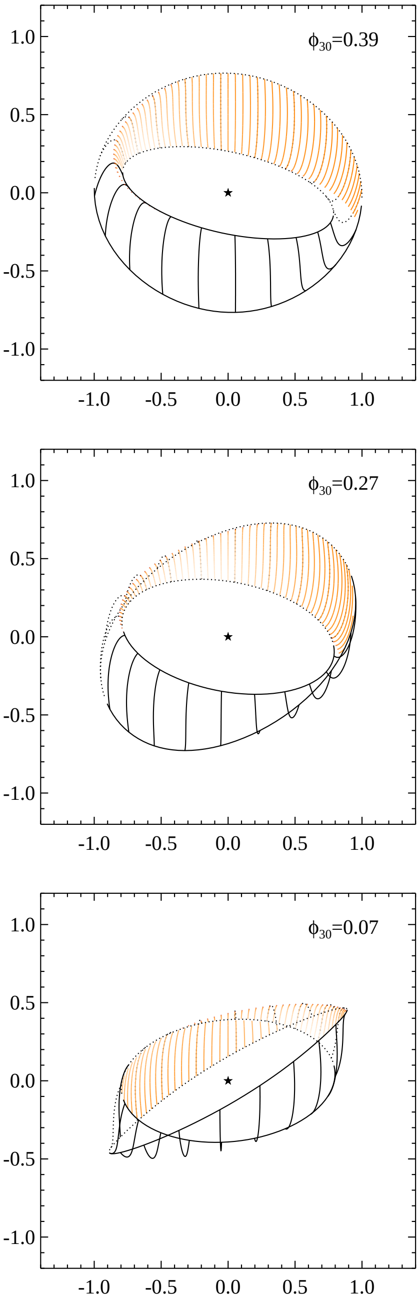

FIG. 11.— Model of the inner regions of a twisted, warped accretion disk, illuminated by the neutron star and observed at three superorbital phases corresponding to the *Suzaku* observations. We set the inclination of the disk to be 70° (van der Meer et al. 2007). The orange shaded regions show areas on the disk which are illuminated by the central star and are visible to the observer.

cessing is a plausible explanation for the observed Fe line emission, although further work is needed to robustly determine the physical origin of the broad feature.

The pulse profiles of LMC X-4 show that the profiles at different energies have different pulse behaviors. In all three observations, the soft (0.5–1 keV) and hard (10–50 keV) profiles show single-peaked, smooth, roughly sinusoidal pulsations. Single-peaked soft pulses have been observed in the well-studied X-ray binary pulsar systems, Her X-1 and SMC X-1 (Zane et al. 2004; Hickox & Vrtilek 2005). Hickox & Vrtilek (2005) using a simple pencil beam model with a twisted inner accretion disk were able to reproduce the observed single-peaked sinusoidal pulsations. We suggest that the soft pulses of LMC X-4 are also due to reprocessing of hard X-rays in the inner accretion disk.

The medium (2–10 keV) component, however, shows single-peaked pulses in observation 1 and double-peaked pulses in observation 2 and (although weakly) in observation 3. Multiple-peaked pulses at $E > 2$ keV have been reported several times in the literature; Woo et al. (1996) observed double-peaked pulses with one dominant peak, while Naik & Paul (2004) and Paul et al. (2002) find pulses with three equally strong peaks. Weak or absent pulsations have also been observed (La Barbera et al. 2001).

Further, the phase shift between the pulsations changes significantly between the three observations. In particular, in observation 1 the pulses in all three bands are largely in phase, while for observations 2 and 3, the hard and soft pulses are almost 180° out of phase, while the medium pulses are shifted somewhat less relative to the soft pulses.

Following previous studies of Her X-1 (e.g., Ramsay et al. 2002; Zane et al. 2004) and SMC X-1 (Hickox & Vrtilek 2005), we attempt to interpret the observed pulse profiles in terms of the soft component being reprocessed emission from the inner disk. We begin by considering a fiducial model for the inner regions of the accretion disk at the superorbital phases of the three observations (Figure 11). The model of a warped, twisted disk is the same as that used by Hickox & Vrtilek (2005) to describe the superorbital variation in SMC X-1[15]. We assume a disk inclination of 70°, consistent with the orbital inclination of LMC X-4 (van der Meer et al. 2007). The area of the disk illuminated by the neutron star is shown in the shaded region. While we do not have strong constraints on the shape of the inner disk for LMC X-4, this model gives us a qualitative picture of what we might expect for reprocessing by a warped, precessing disk.

Another consideration is the geometry of the pulsar beam. For SMC X-1, Hickox & Vrtilek (2005) found that pencil- or fan-shaped beams from the neutron star can provide an acceptable description of the observed pulse profiles, although the pencil beam is preferred at some superorbital phases. For the super-Eddington luminosities observed for SMC X-1 and LMC X-4, theoretical models generally predict that radiation cannot escape from the top of the accretion column and so favor a fan beam emitted from the walls of the column (e.g. Becker 1998; Becker & Wolff 2005). However, fan beam models universally predict a double- or quadruple-peaked hard pulse profile, in contrast to the single peaks observed in LMC X-4. Further, fan beams can occupy a wide and complex range of geometries (for example the reverse fan beam suggested by Scott, Leahy, & Wilson 2000 for Her X-1), and a full treatment requires a detailed description of the accretion flow as well as effects such as gravitational light bending (e.g., Meszaros & Riffert 1988; Leahy 2003). Given these difficulties, in the following discussion we consider only a simple pencil beam and leave a precise determination of the beam geometry for future studies.

Assuming that the radiation pattern consists of two pencil-shaped beams pointing in opposite directions, then if the beams are not exactly in the plane of the accretion disk, one beam will produce a strong observed hard pulse (as we ob-

---

[16] The disk corresponds to the best-fit model for a pencil beam, with parameters given in Table 2 of Hickox & Vrtilek (2005).

serve for LMC X-4) while the other beam may more strongly illuminate the disk. In observation 1, the largest visible area of the disk is almost exactly in the line of sight, and we may expect the hard and soft pulses to be almost in phase with each other. Figure 11 shows that as the disk precesses, the largest visible area of the disk is shifted to the side, which would suggest that the phase shift between the pulsations from the neutron star and those from the reprocessing disk should vary with superorbital phase. This is indeed what we observe for the shift between the medium and soft X-ray pulses (shown in the bottom panel of Figure 10), for which the peak of the cross-correlation increases monotonically between the three observations. Such variations in the $\sim$2–10 keV and $\sim$0.5–1 keV pulse profiles have been interpreted similarly for Her X-1 (Zane et al. 2004) and SMC X-1 (Neilsen et al. 2004).

However, these studies were limited to X-ray data below 10 keV. With the existence of the higher-energy PIN observations, it makes sense to consider the hard (10–50 keV) emission to be the best indicator of the luminosity in the neutron star beam, as the spectrum peaks at these energies. As discussed above, the hard and medium pulses show significantly different behavior. The cross-correlations in Figure 10 indicate that the hard pulses are either close to in phase (observation 1) or close to completely out of phase (observations 2 and 3).

This behavior suggests a different interpretation for the variation in the phase offsets with ϕ_{30}. One idea is that if the beam aligned with the observer also illuminates the largest visible area of the accretion disk, then we might expect the hard and soft pulses to be almost exactly out of phase. It is therefore possible that between observations 1 and 2, the hard X-ray beam and the visible region of the disk moved abruptly relative to each other, thus changing which of the two pulsar beams is illuminating the visible region of the disk. In terms of this picture, the observations would be consistent with a simple "donut" geometry for the reprocessing region, rather than the more complex twisted disk as shown in Figure 11.

We further note that the amplitudes of the soft pulses are equal to or slightly weaker than those of the hard pulses. If the pulses arise from reprocessing, we might expect the reprocessing to blur out the soft profile and thus decrease the amplitude relative to the hard pulses. The observed amplitudes might be explained either if the bulk of the emission comes from a relatively small reprocessing region (as would be suggested by the small inferred $\Omega = 0.05$) and thus limits the blurring of the reprocessed profile. Alternatively, if we are viewing the hard beam from the neutron star off-axis, but the beam strikes the disk directly, then the reprocessing region may see pulsations with a significantly higher amplitude than what we observe.

We conclude that the interpretations regarding the disk and beam geometries are very different depending on whether we consider the $E > 10$ keV X-rays which comprise the bulk of the surface emission from the neutron star. Further, we note that the complex pulse profile and lower pulse fraction in the medium band relative to the hard band suggest that the neutron star emission not be described by a simple pencil beam at all energies. Complex beam shapes have been proposed for some X-ray pulsars; for example, the hard pulses from Her X-1 have been modeled as a central pencil beam surrounded by a fan beam (Blum & Kraus 2000). In our *Suzaku* observations of LMC X-4, the only clear way to explain changes in the medium energy pulse profile (particularly the change from single to double peaks, and the relatively weak pulsations in observation 3) is by intrinsic changes in the beam pattern that move the beam out of our line of sight. Weak or absent pulsations have been observed before in the high state (La Barbera et al. 2001), so perhaps the changes in the beam pattern are fairly common and happen on timescales of $\sim$ weeks.

Despite the difficulty in interpreting the observed pulse profiles, these observations provide further evidence for the soft component originating in a reprocessing disk. As mentioned in Section 3.2, using $R_{\rm BB} \sim 1.5 \times 10^8$ cm and $B \sim 10^{13}$ G, we obtain $R_{\rm BB}/R_m = 0.7$. Keeping in mind that many uncertainties exist in calculating $R_{\rm BB}$ and R_m (such as difficulties in measuring B and the poorly understood interaction of the accretion disk with the magnetic field; see, e.g. Scott et al. 2000; Hickox et al. 2004), the observed correspondence between $R_{\rm BB}$ and $R_{\rm m}$ is rather striking and suggests that the hard X-rays are reprocessed by optically thick material near the magnetosphere.

Finally, we reiterate that the interpretation of disk reprocessing for the soft component is preferred on physical grounds. As discussed in Section 3.2, a thermal bremsstrahlung or MEKAL model (rather than a blackbody) adequately describes the soft spectral component in LMC X-4, but we can rule out this mechanism because it would require too large of an emission region. We conclude, as Hickox & Vrtilek (2005) have inferred for SMC X-1, the soft X-ray component of LMC X-4 is analogous to that of Her X-1 and hence due to reprocessing of hard X-rays by the inner accretion disk.

As an aside, we note that if for LMC X-4 we consider the "hard" flux only at 2–10 keV, we obtain a smaller L_X and thus for $R_{\rm BB}/R_m \sim 0.3$, which is in the range of the values ($R_{\rm BB}/R_m \sim 0.2$–0.4) measured for Her X-1 over similar energy bands (Scott et al. 2000; Hickox et al. 2004). This suggests that $R_{\rm BB}$ may be somewhat closer to $R_{\rm m}$ for Her X-1 as well, if we consider the full luminosity of the hard component which peaks at higher X-ray energies.

A more detailed understanding of the emission from LMC X-4 will require pulse-phase-resolved spectroscopy throughout the superorbital period, as well as a more sophisticated model of the beam and disk geometry. In the future, the *International X-ray Observatory*^{17}, with its greater spectral resolution and effective area, may enable us to undertake detailed, high-resolution pulse-phase spectroscopy and extend our studies to the low state of the superorbital cycle, enabling us to probe further into the accretion mechanism of LMC X-4, and gain a better understanding of accretion in highly magnetized environments.

We are grateful to Joseph Neilsen for his contribution to the data analysis, and Chris Done, Christine Jones, Jonathan McDowell, and Marie Machacek for helpful discussions. We also thank the Suzaku Helpdesk for their valuable advice on the data analysis. The work was supported in part by the National Science Foundation Research Experiences for Undergraduates (REU) and Department of Defense Awards to Stimulate and Support Undergraduate Research Experiences (ASSURE) programs under grant 0754568, Suzaku grant NNX08AI17G, ADP grant NNX08AJ61G, and by the Smithsonian Institution. R.C.H. was supported by an SAO Postdoctoral Fellowship and an STFC Postdoctoral Fellowship.

REFERENCES

Avni, Y. 1976, ApJ, 210, 642
Becker, P. A. 1998, ApJ, 498, 790
Becker, P. A. & Wolff, M. T. 2005, ApJ, 630, 465
Blum, S. & Kraus, U. 2000, ApJ, 529, 968
Boroson, B., Kallman, T., Blondin, J. M., & Owen, M. P. 2001, ApJ, 550, 919
Burderi, L., Di Salvo, T., Robba, N. R., La Barbera, A., & Guainazzi, M. 2000, ApJ, 530, 429
Coburn, W., Heindl, W. A., Rothschild, R. E., Gruber, D. E., Kreykenbohm, I., Wilms, J., Kretschmar, P., & Staubert, R. 2002, ApJ, 580, 394
Davies, S. R. 1990, MNRAS, 244, 93
—. 1991, MNRAS, 251, 64P
Done, C. & Magdziarz, P. 1998, MNRAS, 298, 737
Endo, T., Nagase, F., & Mihara, T. 2000, PASJ, 52, 223
Frank, J., King, A., & Raine, D. J. 2002, Accretion Power in Astrophysics (3rd ed.; Cambridge: Cambridge University Press)
George, I. M. & Fabian, A. C. 1991, MNRAS, 249, 352
Ghosh, P. & Lamb, F. K. 1979, ApJ, 234, 296
Haberl, F. & Pietsch, W. 2005, A&A, 438, 211
Heemskerk, M. H. M. & van Paradijs, J. 1989, A&A, 223, 154
Hickox, R. C., Narayan, R., & Kallman, T. R. 2004, ApJ, 614, 881
Hickox, R. C. & Vrtilek, S. D. 2005, ApJ, 633, 1064
Kelley, R. L., Jernigan, J. G., Levine, A., Petro, L. D., & Rappaport, S. 1983, ApJ, 264, 568
La Barbera, A., Burderi, L., Di Salvo, T., Iaria, R., & Robba, N. R. 2001, ApJ, 553, 375
Lang, F. L., et al. 1981, ApJ, 246, L21
Leahy, D. A. 2003, ApJ, 596, 1131
Levine, A. M., Bradt, H., Cui, W., Jernigan, J. G., Morgan, E. H., Remillard, R., Shirey, R. E., & Smith, D. A. 1996, ApJ, 469, L33
Levine, A. M., Rappaport, S. A., & Zojcheski, G. 2000, ApJ, 541, 194
Meszaros, P. & Riffert, H. 1988, ApJ, 327, 712
Miller, J. M., et al. 2008, ApJ, 679, L113
Mitsuda, K., et al. 2007, PASJ, 59, 1
Naik, S., et al. 2008, PASJ, 60, 237
Naik, S. & Paul, B. 2003, A&A, 401, 265
—. 2004, ApJ, 600, 351
Neilsen, J., Hickox, R. C., & Vrtilek, S. D. 2004, ApJ, 616, L135
Neilsen, J., Lee, J. C., Nowak, M. A., Dennerl, K., & Vrtilek, S. D. 2009, ApJ, 696, 182
Paul, B. & Kitamoto, S. 2002, Journal of Astrophysics and Astronomy, 23, 33
Paul, B., Nagase, F., Endo, T., Dotani, T., Yokogawa, J., & Nishiuchi, M. 2002, ApJ, 579, 411
Ramsay, G., Zane, S., Jimenez-Garate, M. A., den Herder, J., & Hailey, C. J. 2002, MNRAS, 337, 1185
Rivers, E., et al. 2010, ApJ, 709, 179
Saez, C., Chartas, G., & Brandt, W. N. 2009, ApJ, 697, 194
Scargle, J. D. 1982, ApJ, 263, 835
Scott, D. M., Leahy, D. A., & Wilson, R. B. 2000, ApJ, 539, 392
Swank, J. H. 2006, Advances in Space Research, 38, 2959
Tsygankov, S. S. & Lutovinov, A. A. 2005, Astronomy Letters, 31, 380
van der Meer, A., Kaper, L., van Kerkwijk, M. H., Heemskerk, M. H. M., & van den Heuvel, E. P. J. 2007, A&A, 473, 523
Vrtilek, S. D., Raymond, J. C., Boroson, B., & McCray, R. 2005, ApJ, 626, 307
White, N. E. 1978, Nature, 271, 38
Woo, J. W., Clark, G. W., Levine, A. M., Corbet, R. H. D., & Nagase, F. 1996, ApJ, 467, 811
Yaqoob, T. 1998, ApJ, 500, 893
Yaqoob, T., Edelson, R., Weaver, K. A., Warwick, R. S., Mushotzky, R. F., Serlemitsos, P. J., & Holt, S. S. 1995, ApJ, 453, L81+
Zane, S., Ramsay, G., Jimenez-Garate, M. A., Willem den Herder, J., & Hailey, C. J. 2004, MNRAS, 350, 506

---

[18] http://ixo.gsfc.nasa.gov